



Full length article

Impacts of kerogen type and thermal maturity on methane and water adsorption isotherms: A molecular simulation approach

Isa Silveira de Araujo, Archana Jagadisan, Zoya Heidari *

Department of Petroleum and Geosystems Engineering, The University of Texas at Austin, 200 E Dean Keeton St, Austin, 78712, TX, United States

ARTICLE INFO

Keywords:

Kerogen
Adsorption
Methane
Geochemistry
Molecular simulation
EOR in shale

ABSTRACT

The molecular structure of kerogen is known to control the type, amount of petroleum generated as well as its interaction with reservoir fluids. The adsorption behavior of kerogen with respect to reservoir fluids can enhance our understanding of kerogen wetting properties. Therefore, quantifying the governing factors controlling the adsorption of water and methane in organic pores is critical in understanding fluid flow and adsorption phenomena in organic-rich mudrocks. In this paper, we perform molecular simulations (MS) and quantify water and methane adsorption isotherms on kerogen pore surfaces for the purpose of investigating the impact of kerogen molecular structure on kerogen-fluid interfacial interaction. To realistically represent kerogen structures, we use different kerogen molecular models to emulate kerogen of different types and thermal maturity. The kerogen molecules are condensed to form a porous kerogen structure. The Grand Canonical Monte Carlo simulation (GCMC) method is applied to calculate adsorption isotherms of methane and water molecules in kerogen nanopores. We compute the adsorption behavior of water and methane molecules on type I, II and III kerogen samples. The molecular simulations of increasing thermal maturity from IIA to IID at low pressures (less than 10 MPa) and temperature of 300 K in type II kerogen resulted in increasing methane adsorption capacity. At 5 MPa, the methane adsorption relatively increased 81% from IIA to IID. The adsorption capacity of methane is also shown to increase from type IA to IIA to IIIA. Similarly to methane, water adsorption capacity is found to increase from type IA to IIA to IIIA. However, water adsorption capacity on kerogen of different thermal maturity increases from IIB to IIA. Kerogen structures of types IID and IIC show very similar adsorption capacity nearly overlapping at four different pressures. However, water adsorption on IID and IIC kerogen is still found to be smaller compared to IIA and IIB. The outcomes of this work contribute to improving the understanding of the impact of kerogen molecular structure on adsorption of fluids on kerogen surfaces. Moreover, it can provide insights into fluid mobility assessments in organic-rich mudrocks by providing information about the adsorbed gas content on kerogen surfaces.

1. Introduction

Organic-matter-hosted porosity contributes to a significant portion of the total porosity in organic-rich mudrocks especially at higher thermal maturity. The organic matter in these rocks is mainly composed of kerogen and is considered the main source of adsorbed gas. Kerogen is classified based on (i) initial structure and chemistry, and (ii) degree of thermal alteration (called thermal maturity). Four types of kerogen can be identified based on the origin and geochemistry of the organic material, which include:

- type I kerogen, which is typically formed in lacustrine anoxic environment,
- type II kerogen from marine shale and continental planktons,
- type III kerogen from terrestrial organic matter, and

- IV from older sediments redeposited after erosion.

The elemental ratios of hydrogen/carbon (H/C) and oxygen/carbon (O/C) varies with the type of kerogen and are associated with changes in its structure [1,2]. Sulfur and nitrogen are also other elements found in kerogen structure. Sulfur is usually associated with type II kerogen. This component can be found in organic structures of kerogen as aliphatic sulfur and thiophenic rings. Sulfur content decreases with increasing source rock thermal maturity, as a result of dilution by further generation of non-sulfur compounds as well as by removal of sulfur. Sulfur can be lost as H_2S and also due to the retention of sulfur in insoluble reservoir bitumen or pyrobitumen [3]. Nitrogen is present primarily in the form of pyrrolic pyridinic and protonated basic nitrogen structures. Kelemen et al. [4] characterized several kerogen

* Corresponding author.

E-mail address: zoya@utexas.edu (Z. Heidari).

samples and found that the content of pyridinic/protonated-basic nitrogen is comparable regardless of the thermal maturity level. Thermal maturation of kerogen leads to change in its chemical composition and pore structure. Increasing thermal maturity of kerogen results in transformation of kerogen geochemistry from hydrogen-rich organic matter into hydrogen-poor residual carbon resulting in marked decreases in H/C ratio [5]. Moreover, the aromaticity of kerogen also increases with increasing thermal maturity, transforming kerogen to graphitic structure with higher aromatic sp² hybridized carbon [6]. Kerogen structure condenses to mainly graphitic structure with aromatic units of sp² hybridized carbons [7]. The structure and pore characteristics of any given kerogen is a function of the type of kerogen and thermal maturity.

Investigating the adsorption behavior of kerogen with respect to reservoir fluids can enhance our understanding of kerogen wetting properties and is essential for evaluation of shale gas-in-place and well productivity. Information about water adsorption on kerogen at different thermal maturity levels is of great relevance to processes such as CO₂ storage. In such applications, the content of preadsorbed water on kerogen can affect CO₂ distribution and adsorption. It can also block the nanochannels affecting gas flow transport behavior of fluids [8]. Moreover, the presence of moisture in kerogen can affect the efficiency of enhanced oil recovery (EOR) processes in shale. Therefore, the development of optimal field CO₂ injection processes for shale oil recovery requires understanding of the water adsorption characteristics of kerogen considering the influence of thermal maturity and type. Quantification of the governing factors controlling the adsorption of water and methane in organic pores is critical in understanding fluid flow and adsorption phenomena in organic-rich mudrocks.

Adsorption is a complex process that can be controlled by several factors such as pressure, temperature, and the nature of the fluid-solid system. Other parameters such as pore type and diameter are also known to affect the adsorption process. For instance, experimental analyses have shown that higher temperature results in a lower gas sorption content in the Devonian shale reservoir due to the exothermic nature of physical adsorption [9]. Studies of water adsorption on porous carbon suggests that the vapor-liquid critical temperature for water in hydrophobic nanotubes decreases as the pore diameter narrows [10]. Another important factor that strongly impacts water adsorption is the presence of secondary adsorption sites. Shale rocks are examples of adsorbent with primary and secondary sites. The primary sites refer to hydrophilic nanopores, while secondary sites refer to both the adsorption sites formed above the previously-occupied sites with weak binding energies and adsorption sites in the hydrophobic nanopores. Since water molecules preferentially adsorb on higher energy sites, at low relative pressure, most of sites utilized are the primary sites [11]. Understanding the synergistic effect of all the parameters affecting water and methane adsorption on kerogen can provide insights into fluid mobility assessment in organic-rich mudrocks.

Reliable experimental studies on the kerogen adsorption are rare because of the challenges in retaining the microstructure of kerogen in the extraction process [12]. To avoid these challenges, MD simulation has become more common to gain an understanding on the kerogen microstructure and adsorption mechanisms [12–24]. Several publications on kerogen adsorption adopt kerogen models developed by Ungerer et al. [2] to construct kerogen matrix structure.

Vasileiadis et al. [22] performed GCMC simulations to determine the impact of porosity on methane adsorption for high thermal maturity type II kerogen molecules. They found that the methane-accessible surface area increased with increasing the number of kerogen macromolecules. Sui et al. [8], Huang et al. [25], Zhao et al. [24], and Sui and Yao [13] showed that an increase in thermal maturity of kerogen samples increase the methane adsorption. Tesson and Firoozabadi [12] showed using type IIA kerogen that the surface roughness and chemical composition can affect the adsorption in kerogen slit pores. Most of the previous publications focus on a single type of kerogen molecule and

there is limited data on how different kerogen types can impact the adsorption in kerogen nanopores.

Zhao et al. [24] and Huang et al. [25] determined that methane adsorption capacity decreases with increasing moisture content in kerogen samples. However, recent studies on wettability of kerogen to water showed that it varies with thermal maturity as well. Therefore, the moisture content in the samples would also vary with thermal maturity. This has not been considered in the aforementioned studies. Zhao et al. [24] showed that in type II kerogen sample, the competitive adsorption simulation results indicate that kerogen prefers to adsorb water (H₂O) over CH₄. However, there are very few studies on the impact of kerogen geochemistry on water adsorption and furthermore moisture content data used to calibrate kerogen simulations are mainly from empirical results.

Published work to date suggests that it is important to quantify the impacts of kerogen type and thermal maturity on water adsorption to gain a better understanding of the moisture content present in kerogen, and thus predict more reliable gas adsorption on kerogen. In this paper, we apply molecular simulation methods to evaluate the methane and water adsorption capacity of kerogen structures. We perform molecular dynamics simulation, grand canonical Monte Carlo simulations and use the Widom insertion method to (i) investigate the impact of kerogen type and thermal maturity on methane adsorption capacity, (ii) investigate the impact of kerogen type and thermal maturity on water adsorption capacity, and (iii) determine the impact of reservoir temperature on methane adsorption capacity of kerogen.

2. Methods

In this section, we describe the details of the molecular simulation methods used in this study. First, MD simulations are used to generate dense kerogen structures from individual molecular models of type I, II and III kerogens. For type II kerogen, four different kerogen molecules were used, representing a wide range of thermal maturity (i.e., IIA (lowest), IIB, IIC, and IID (highest)). Fig. 1 shows the proposed workflow for obtaining the condensed kerogen structures. Then, GCMC simulations were performed to characterize the properties of the porous structures present in the organic matter and obtain the adsorption capacities.

2.1. Construction of kerogen molecular structures

Ungerer et al. [2] selected six kerogen samples from the work of Kelemen et al. [4] with the objective of representing the three main organic types as well as variations in kerogen thermal maturity. After selecting the kerogen samples, they developed kerogen model units for each kerogen type based on the elemental analysis and functional group analysis documented in the work of Kelemen et al. [4]. The kerogen molecular models developed by Ungerer et al. [2] are used for simulating the adsorption behavior of methane and water molecules in this paper. According to Kelemen et al. [4], the type II kerogen samples selected span the range from immature to postmature (i.e., approximately 0 to 95% conversion), while type IIIA span the oil window (i.e., approximately 10 to 60% conversion). The remaining sample (i.e., type I kerogen) is immature with respect to oil generation. Table 1 summarizes the hydrogen index (HI), the temperature at which the maximum rate of hydrocarbon generation occurs (T_{max}) reported in the work of Kelemen et al. [4] as well as the approximate range of vitrinite reflectance obtained from Van Krevelen diagram for each kerogen type. This data helps to better distinguish the thermal maturity level of the kerogen structures documented in this paper.

Table 1: Kerogen Rock-Evaluation Pyrolysis Data obtained from Kelemen et al. (2007) and vitrinite reflectance from Van Krevelen diagram

Sample	T _{max} (°C)	Hydrogen Index (HI)	Vitrinite Reflectance
Kerogen IA	446	739	0.4-0.5%
Kerogen IIA	414	532	0.4-0.5%
Kerogen IIB	438	439	0.5-1.0%
Kerogen IIC	443	242	1.0-1.5%
Kerogen IID	479	22	1.5-2.0%
Kerogen IIIA	427	295	0.4-0.5%

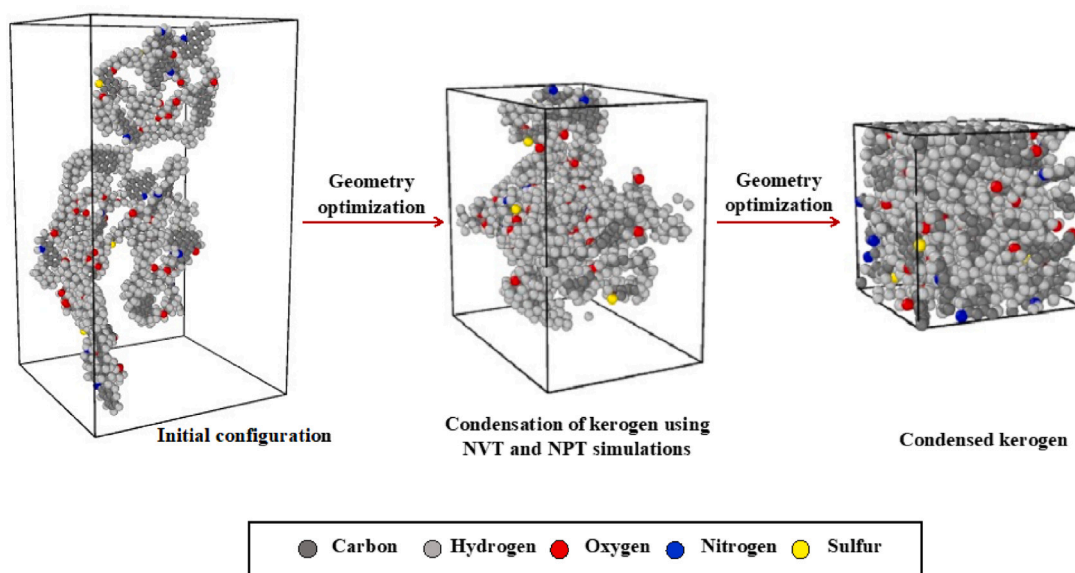


Fig. 1. Workflow for obtaining condensed kerogen structures.

Table 2 shows the composition, structural parameters, density, maximum pore size, and pore volume for each one of the of kerogen molecular models used in this work. Amongst the three types of kerogen, type I (IA), type II (IIA), and type III (IIIA), the O/C ratio is the lowest for IA kerogen (O/C-0.052), followed by IIA (O/C- 0.095), and the highest for IIIA kerogen (O/C-0.116). Aromaticity also follows a similar trend with the highest aromaticity among the three types of kerogen found in IIIA kerogen at 57%, followed by IIA at 41% and IA kerogen at 29%. The impact of thermal maturity in type II kerogen is a decrease in O/C ratio from 0.095 to 0.051 and increase in aromaticity from 41% to 79% from IIA to IID. The size of the generated kerogen model used for the simulation can have an impact on the properties studied. In previous studies [2,26,27], kerogen structures were simulated using 4 kerogen molecules and these studies showed that there were qualitative and quantitative agreements between molecular and experimental data on the adsorption capacity and density.

Table 2: Characterization of kerogen molecules used in this paper

Structural features of the kerogen model unit documented in Ungerer et al. (2015)	Kerogen Model Parameters	Kerogen IA	Kerogen IIA	Kerogen IIB	Kerogen IIC	Kerogen IID	Kerogen IIIA
	H/C	1.53	1.17	1.12	0.90	0.58	0.886
Computed parameters of the kerogen structures from molecular simulations	O/C	0.052	0.095	0.060	0.054	0.051	0.116
	N/C	0.028	0.024	0.022	0.021	0.023	0.017
	S/C	0.012	0.012	0.009	0.008	0.010	0.000
	Aromaticity (%)	29%	41%	45%	58.7%	79%	57%
Computed parameters of the kerogen structures from molecular simulations	Non-aromatic carbon (%)	71%	59%	55%	41.3%	21%	43%
	Aliphatic S (%)	67%	33%	50%	50%	0%	-
	Density (g/cm ³)	1.05	1.13	1.18	1.23	1.26	1.24
	Total Pore Volume (cm ³ /g)	0.197	0.226	0.269	0.327	0.264	0.288
Computed parameters of the kerogen structures from molecular simulations	Max Pore size (Å)	7.29	6.63	6.57	12.51	9.15	7.29

Dense kerogen structures are generated by using the process of annealing where the kerogen molecules are packed in a simulation cell and compressed at 20 MPa with starting temperatures of 900 K which are decreased to 300 K. For simulations in this study, the process described in Collell et al. [28] is used to generate the condensed structures of kerogen. The MD simulations are performed in the LAMMPS software [29] and the consistent-valence forcefield (CVFF) [30] is used to represent the interatomic interactions in the kerogen molecules. Lennard-Jones (LJ) 6/12 is used to represent the dispersion/repulsion with a cutoff distance of 9.5 Å. Finally, coulombic interactions and long-distance corrections are used to estimate LJ energy beyond the cutoff distance. Four molecules of kerogen are placed in a simulation box of size 100 × 100 × 100 Å³. NVT (constant number volume and temperature) simulations are then performed at 900 K for 200

ps. Subsequently, NPT (constant number pressure and temperature) simulations with pressure of 20 MPa and decreasing temperatures from 900 K to 300 K are performed for a total of 1200 ps. During the compressing process, a high pressure needs to be imposed to prevent the system from expanding as a low-density gas, and a decrease in temperature from 900 K to 300 K is required to reduce the density of the structure and to reach the desired kerogen density values. A timestep of 1 fs is used for the simulations. The density of the resultant kerogen structures ranges from 1.05 to 1.26 g/cc, which agrees with the experimentally observed density [31,32].

2.2. Adsorption simulations

The GCMC simulation is widely used to model the adsorption properties of fluids and mixtures in porous materials. In the grand-canonical ensemble (μ VT ensemble), the temperature, volume, and chemical potential are fixed, while the number of molecules in the adsorbed phase is allowed to fluctuate. Insertion and deletion moves are used in the μ VT ensemble to equilibrate the system at the defined value of the chemical potential [33]. In this paper, GCMC simulations are applied to compute absolute adsorption isotherms of pure methane and water on kerogen matrix. The simulations are performed using RASPA, a molecular simulation software [34]. The methane molecules are modeled by Transferable Potentials for Phase Equilibria Force Field (TRAPPE)-United Atom force field [35]. The interaction between methane molecules and kerogen are described using the Lennard-Jones potential and Lorentz-Berthelot mixing rules [36,37]. The water molecules were described by applying the Simple Point Charge (SPC) force field [38] and the interactions between water and kerogen molecules were also modeled using the Lennard-Jones potential and Lorentz-Berthelot mixing rules. The adsorption of methane was evaluated at the temperature of 300 K and pressure range of (1 MPa to 20 MPa) on the following kerogen types: IA, IIA, IIB, IIC, IID and IIIA. The pressure range of 1–20 MPa was chosen with the objective of evaluating the adsorption behavior of both water and methane at low and high pressure conditions. This pressure range includes the pressure conditions usually found in oil and gas reservoirs. The effect of temperature on the adsorption behavior of kerogen IIC was evaluated by performing GCMC simulation at temperatures of 300 K, 330 K and 360 K and pressure range of (1 MPa to 20 MPa). Each GCMC simulation run consist of 1 × 10⁶ equilibration steps and 1 × 10⁶ production steps for methane/kerogen systems and 1 × 10⁶

equilibration steps and 2×10^6 production steps for water/kerogen systems. The Langmuir model was adopted model to describe the methane and water adsorption processes on kerogen structures in this paper. The mathematical expression of Langmuir isotherm is given by

$$q_e = q_{\max} \frac{KP}{1 + KP}, \quad (1)$$

where, q_e is the amount of the adsorbate adsorbed (mmol/g) and P is the pressure (MPa). The parameters q_{\max} and K , are the Langmuir constants. q_{\max} (mmol/g) is represented as the maximum monolayer adsorption capacity and K (MPa⁻¹) is related to the binding energy of the adsorption system

2.3. Pore-size distribution

The pore-size distributions (PSD) for the kerogen structures are calculated in RASPA using the method described in Gelb and Gubbins [39]. The principle of this method is that for every point in the void volume, the largest sphere that encloses the point and does not overlap with any of the kerogen atoms is determined. Combining all such spheres for the whole structure gives the pore-size distribution of that structure. The cumulative pore volume curve is then obtained from integrating through the pore-size distribution curve [34]. The surface area of each kerogen sample was computed by performing Monte Carlo (MC) simulations. In these simulations, a probe molecule (nitrogen) is rolled along the surface of the framework to compute the surface area [34].

3. Results

3.1. Impact of thermal maturity of kerogen on methane adsorption

The ability of a porous solid to adsorb molecules depends greatly on the pressure, temperature and chemistry of the adsorbent (framework) and adsorbate. First, we analyze the methane adsorption capacity of Type II kerogen at different thermal maturity levels. Fig. 2 shows the kerogen structure obtained by molecular simulations and the configuration of the methane molecules within kerogen pores. Fig. 3 shows the absolute adsorption isotherms simulated for each one of the four kerogen type II structures (i.e., IIA, IIB, IIC, and IID) at the temperature of 300 K and pressure range of 1 MPa to 20 MPa. Analyzing the results in the pressure range of 1 MPa to 11 MPa, we observe that the methane adsorption capacity by kerogen type follow the order IIA, IIB, IIC, and IID, where IIA presents the lowest loading of methane molecules and IID the highest loading of methane. From 11 MPa to 20 MPa, methane adsorption capacity remains on the same order for IIA and IIB (with higher methane adsorption capacity for IIB as compared to IIA), but we see that IIC shows slightly higher methane adsorption capacity compared to IID. The results of methane adsorption capacity at a fixed pressure and temperature (5 MPa and 300 K) show an increase from 2.13 mmol/g for type IIA kerogen to 2.78 mmol/g for type IIB kerogen. It further increases to 3.44 mmol/g for type IIC kerogen and 3.86 mmol/g for type IID kerogen. From Table 1, we see that as thermal maturity increases, the aromaticity increases along with total pore volume and maximum pore size except for the type IID kerogen. This suggests a synergic effect of aromaticity, pore volume, and pore-size distribution on methane adsorption on kerogen structures. According to [40], the aromatic rings present in kerogen tends to resist deformation during the condensation process required to create porous kerogen structures from single kerogen molecules. As a result, the pore space created is increased in kerogen samples with high aromatic content, such as highly mature kerogen samples. This process will result in higher pore space accessible to the adsorbate. At pressures higher than 11 MPa, we see that the methane adsorption capacity of kerogen sample IIC is higher than that of IID. The greater total pore volume and thus pore surface area in IIC kerogen, may explain why the methane adsorption capacity is higher in IIC kerogen than in IID kerogen rather than aromaticity controlling the behavior.

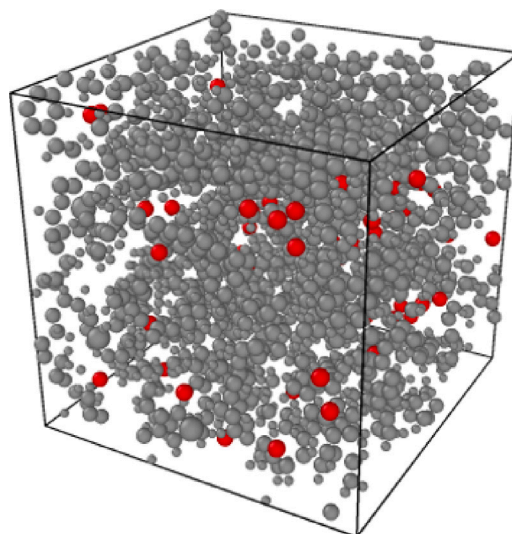


Fig. 2. Screenshot of GCMC simulation of methane adsorption on kerogen. The grey spheres represent kerogen (adsorbent) and red spheres represent methane (adsorbate). (For interpretation of the references to color in this figure legend, the reader is referred to the web version of this article.)

3.2. Impact of kerogen type on methane adsorption

Next, we analyze the methane adsorption capacity of different kerogen types. Fig. 4 shows the methane adsorption isotherms for kerogen types IA, IIA and IIIA at 300 K. The results show that the adsorbed amount of methane increases from kerogen type IA to IIA and to IIIA. At 20 MPa, the adsorption capacity of methane increases from 2.23 mmol/g for kerogen type IA to 3.33 mmol/g for type IIA kerogen. There is a sharp increase in methane adsorption to 6.46 mmol/g at 20 MPa for type IIIA kerogen. The results show that methane adsorption on different kerogen types is correlated to the aromaticity of the kerogen structures, similar to what we observed in the type II kerogen of different thermal maturities. This indicates that the adsorption capacity also correlates to kerogen geochemistry. Type I kerogen is the structure with highest H/C ratio (1.53) and the lowest O/C ratio (0.052). However, an increase in thermal maturity leads to chemical loss of H resulting in an increase in aromaticity from 29% in type IA kerogen to 57% in type IIIA kerogen. The increase in aromaticity and decrease in O/C ratio results in higher methane adsorption capacity. that the adsorption capacity also correlates to kerogen geochemistry. Fig. 5 shows the correlation between methane adsorption capacity, aromaticity and O/C ratio for different kerogen types. The results show that methane adsorption on different kerogen types is correlated to the aromaticity of the kerogen structures, similar to what we observed in the kerogen type II of different thermal maturity levels. This observation indicates that the adsorption capacity is correlated to kerogen geochemistry. Type I kerogen is the structure with highest H/C ratio (1.53) and the lowest O/C ratio (0.052). However, an increase in thermal maturity leads to chemical loss of H, resulting in an increase in aromaticity from 29% in type IA kerogen to 57% in type IIIA kerogen. The increase in aromaticity and decrease in O/C ratio results in higher methane adsorption capacity. Fig. 6 shows the correlation between methane adsorption capacity and total pore volume for different kerogen types. We observe that the methane adsorption capacity is also directly correlated to the total pore volume of the structures. This observation suggests that both structural and chemical features of the kerogen structures govern methane adsorption on kerogen structure.

3.3. Impact of temperature on methane adsorption

To evaluate the impact of temperature on methane adsorption on kerogen surfaces, adsorption of type IIC kerogen is simulated at

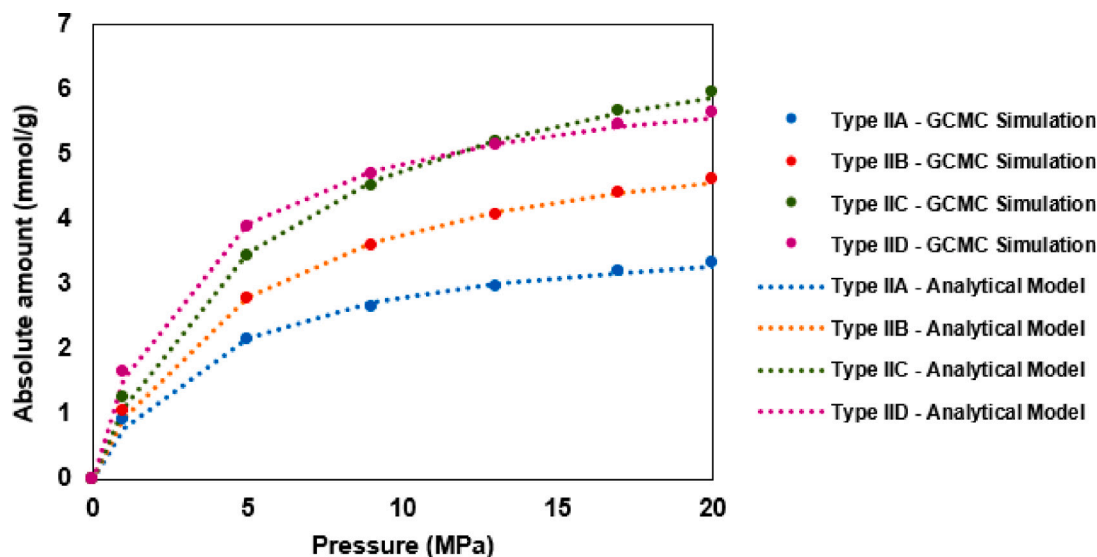


Fig. 3. Methane adsorption isotherms at 300 K for kerogen type II at different thermal maturity levels.

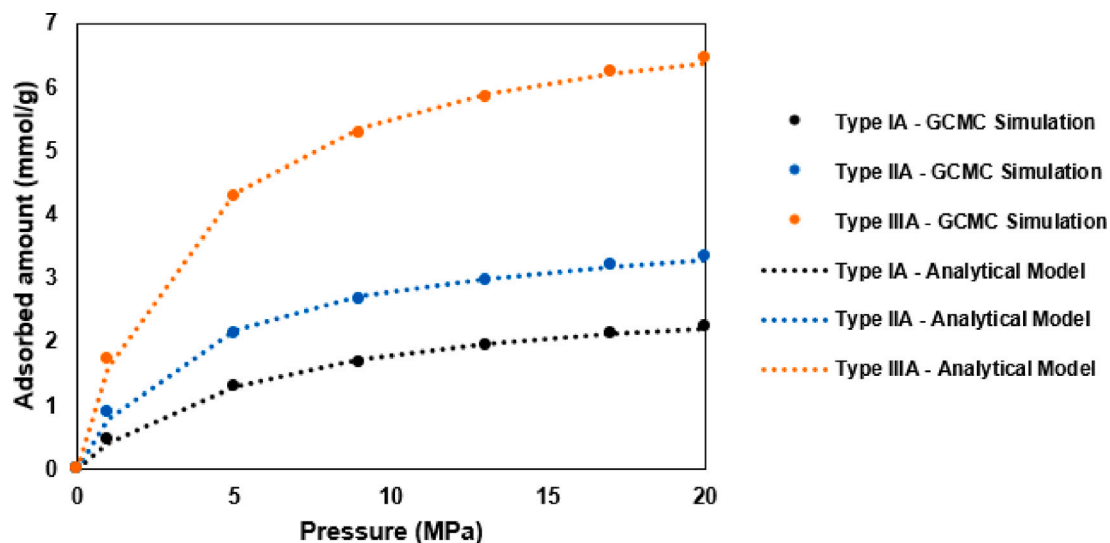


Fig. 4. Methane adsorption isotherms at 300 K for different kerogen types.

different pressures. Fig. 7 displays the methane absolute adsorption isotherms for type IIC kerogen at temperatures 300 K, 330 K and 360 K. The simulations show that adsorption of methane (at 20 MPa) decreases by 25% as temperature increases from 300 K to 360 K. This observation is explained by the fact that methane adsorption on kerogen surface is an exothermic process [41]. Hence, we observe in our simulations that an increase in temperature leads to a decrease in methane adsorption capacity.

3.4. Impact of kerogen geochemistry on water adsorption

To have a better understanding of the affinity between water and kerogen, GCMC simulations were performed and water adsorption isotherms were calculated at 300 K. Figs. 8 and 9 compare the estimated values of water adsorption at different thermal maturity levels and types of kerogen, respectively.

Analyzing the shape of water and methane adsorption isotherms, we find that they correspond to Type I isotherms according to IUPAC definition [42]. Type I isotherms rise steeply at low pressures and reach a plateau. They are obtained when performing adsorption on

microporous adsorbents. According to Rouquerol et al. [43], type I(a) corresponds to the filling of narrow micropores. Analyzing methane and water isotherms, we conclude that water adsorption in kerogen leads to a quick filling of these micropores compared to methane. This pore filling is explained by the formation of cluster-like water molecular assemblies. This phenomenon has been observed in microporous structures of activated carbon containing different functional groups. Dubinin and Serpinsky [44] proposed the cluster formation mechanism to explain the steep uptakes of water in the adsorption isotherms. Muller et al. [45] showed in their studies that the adsorption of water on carbon does not proceed in an orderly monolayer-multilayer form. They report that first, water adsorbs preferentially on particular sites, subsequently, these adsorbed water molecules act as nucleation sites for the further adsorption of molecules, leading to the formation of three-dimensional clusters. Thus, spontaneous pore filling precedes the formation of a hypothetical monolayer.

Comparing the adsorption isotherms of methane and water, we observe that in general at same temperature and pressure conditions, kerogen can adsorb more methane than water molecules. Evaluating the impact of thermal maturity on water adsorption, we found that

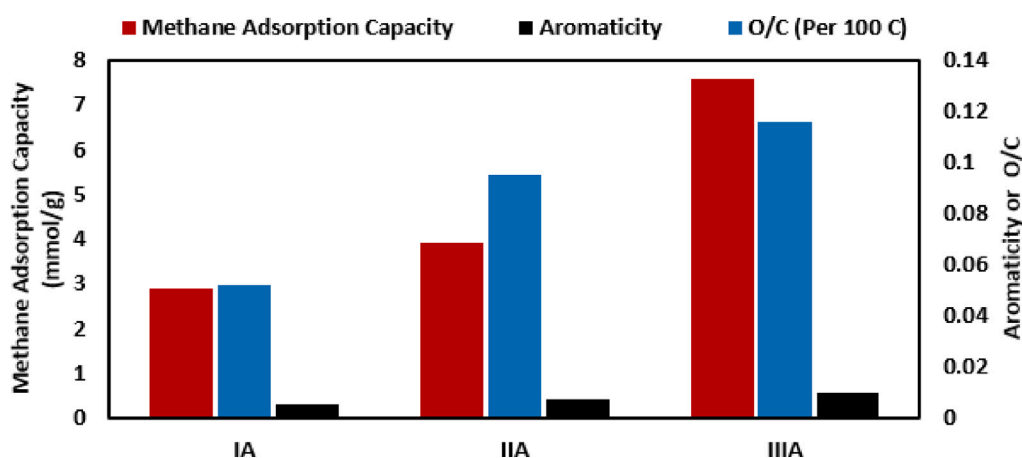


Fig. 5. Correlation between methane adsorption capacity, aromaticity, and O/C ratio for different kerogen types.

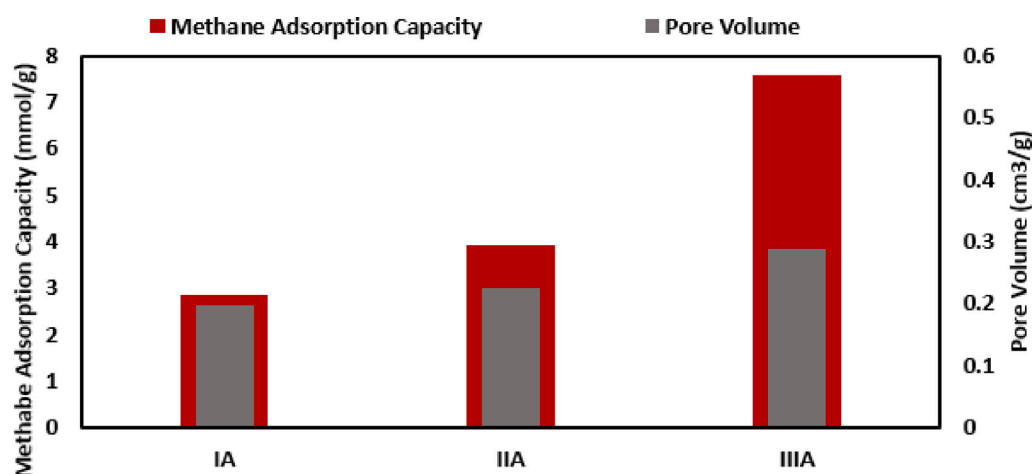


Fig. 6. Correlation between methane adsorption capacity and total pore volume for different kerogen types.

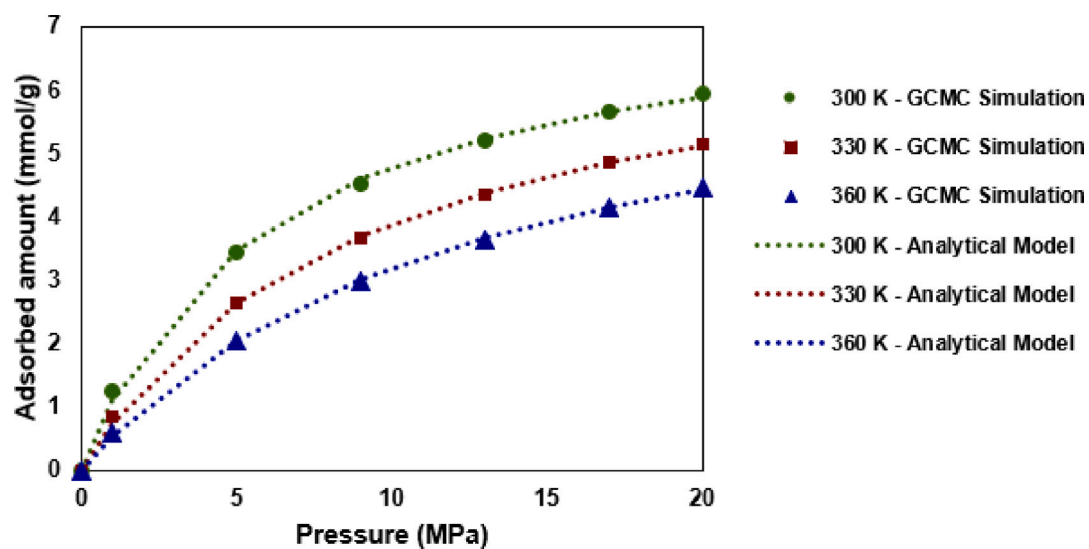


Fig. 7. Methane adsorption isotherms for kerogen type IIC at 300 K, 330 K and 360 K.

an increase in thermal maturity from IIA to IIB decreases the water adsorption capacity. In other words, the affinity between kerogen and water is decreased when thermal maturity is increased. As expected, this behavior is the opposite of what is observed in Fig. 3 where we show that methane adsorption capacity in kerogen IIA is the lowest. Although kerogen IIA and IIB have smaller pore size compared to kerogen IIC and IID, they present higher water adsorption capacity. This observation confirms that water adsorption on kerogen IIA and IIB is mainly controlled by the kerogen geochemistry. Kerogen IIC and IID simulations show smaller water adsorption capacity compared to IIA and IIB due to their higher thermal maturity. However, water adsorption isotherm curves for kerogen IIC and IID overlap in four different pressure points. The water adsorption capacity of kerogen IIC and IID results from an interplay of kerogen geochemistry and pore size distribution. The lower affinity between kerogen and water at higher thermal maturity has also been confirmed by the experimental contact angles of water droplets on kerogen surfaces, documented in the work of Jagadisan and Heidari [46]. In their work, kerogen samples were synthetically matured to obtain kerogen at different maturity levels. They reported that in a nonheated kerogen sample (at low thermal maturity level) the contact angle to water was 44° (water-wet kerogen), while a sample heat-treated at 650° F (at high thermal maturity level) had a contact angle of 122° (oil-wet, i.e., water is the non-wetting phase). A possible explanation for the hydrophilic behavior of kerogen at low thermal maturity is related to the fact that these structures have more aliphatic carbons and polar small-molecule chains. Therefore, kerogen at low thermal maturity levels has higher affinity to water molecules, which makes it water-wet.

Table 3 lists the Langmuir constants K (MPa⁻¹) computed from water and methane adsorption isotherms on kerogen structures at different thermal maturities. We observe that this parameter is higher for water molecules compared to methane. This observation indicates that water molecules bind strongly to kerogen surface, while methane molecules bind weakly. This result indicates that the presence of some functional groups associated with oxygen for instance, results in strong water attraction to the surface and can possibly cause changes in the wettability of kerogen.

Table 3: Langmuir constants K (MPa⁻¹) computed from water and methane adsorption isotherms on kerogen structures at different thermal maturity levels

	Water- K (MPa ⁻¹)	Methane- K (MPa ⁻¹)
IIA	11.99712416	0.250223085
IIB	10.43401957	0.191611955
IIC	2.446425374	0.166683057
IID	4.245189424	0.311107787

Fig. 9 shows the impact of different kerogen types on water adsorption capacity. The results show that kerogen type IA has the lowest adsorption capacity and kerogen IIIA the highest adsorption capacity. This result follows the same trend observed in adsorption isotherms of methane in different kerogen types (Fig. 4). This observation suggests that pores size distribution is a dominant factor controlling the adsorption in different kerogen types.

3.5. Pore-size distribution of kerogen structures

Figs. 10 and 11 show the pore-size distributions and cumulative pore volume of the kerogen structures. The results from Fig. 8 shows that kerogen samples IIA, IIB, and IID indicate a pore-size distribution of less than 10 Å. However, kerogen IIC shows pore sizes larger than 10 Å. Moreover, the cumulative pore volume indicates a higher pore volume for IIC kerogen as compared to other kerogen samples of type II. This indicates that type IIC kerogen contains larger total pore volume and larger pores sizes available for adsorption. Similar to Fig. 9, type

IIIA kerogen shows higher pore volume compared to that of type IA and IIA.

A comparison of the calculated surface area for each kerogen structure and the total pore volume is displayed in Fig. 12. We observe that surface area and pore volume follow similar trends for all kerogen types, indicating that the total pore volume available for adsorption is directly correlated to the total surface area.

4. Conclusions

In this work, molecular simulations were performed to investigate the adsorption behavior of methane and water on kerogen surfaces. The kerogen structures analyzed are types I, II, and III. To evaluate the impact of thermal maturity on methane and water adsorption, kerogen type II at increasing thermal maturity level (i.e. IIA, IIB, IIC and IID) were also analyzed.

The results showed that the methane and water adsorption capacity of kerogen is strongly related to both its geochemistry and structural aspects such as pore size distribution and available total pore volume. Analyzing the results of methane adsorption on type II kerogen at different thermal maturity levels, we found that at low pressures, methane adsorption capacity increases with an increase in thermal maturity from kerogen type IIA to IID. However, at pressures higher than 11 MPa, kerogen type IIC has slightly higher methane adsorption than kerogen type IID. This observation could be attributed to secondary adsorption in larger pores in IIC kerogen structure, originating from the annealing process of kerogen. From the results of water adsorption isotherms on same kerogen samples, we found that water adsorption on kerogen type IID and IIC is approximately the same. However, higher thermal maturity kerogen such as IID and IIC presented a lower water adsorption compared to that of IIA and IIB. In general, we conclude that highly mature kerogen has stronger affinity to methane (compared to water) and less affinity to water (compared to methane). This suggest that the kerogen samples have different wetting properties and that the mature kerogen samples are likely to be more oil-wet. Additionally, we found that methane adsorption on kerogen samples with different thermal maturity levels is synergically controlled by aspects of kerogen geochemistry such as O/C ratio and aromaticity as well as other properties such as pore size and pore volume. Further investigations are needed in order to understand which of these parameters impacts the most on methane adsorption. We observed that in the case of water adsorption, kerogen structure with small pore volume, such as IIA, show the highest water adsorption. This observation suggests that geochemistry is the primary factor controlling water adsorption.

Results also demonstrated that kerogen type also significantly affects water and methane adsorption. Water adsorption capacity of different kerogen types decreases from kerogen type IIIA to IIA to IA. The same trend was observed in methane adsorption isotherms of kerogen of different types. These observations suggest that the pore-size distribution is a dominant factor controlling adsorption capacity of different kerogen types. To evaluate the impact of temperature on methane adsorption on kerogen surface, methane adsorption on kerogen type IIC was simulated at 300 K, 330 K and 360 K. Comparing the isotherms computed for kerogen IIC at different temperatures, we found that an increase in temperature resulted in a decrease in methane adsorption capacity of kerogen.

A significant amount of simulation efforts has been devoted to understand the correlation between structure of the host kerogen and the amount and composition of the gas trapped in its structure. However, modeling such a complex material can be very challenging. Hence, underlying assumptions and simplifications are made for modeling such rock components. For instance, most of the kerogen models used in molecular simulations show only ultra-microporosity. Nevertheless, kerogen structures also include mesopores what can highly influence in methane adsorption capacity as well as fluid mobility.

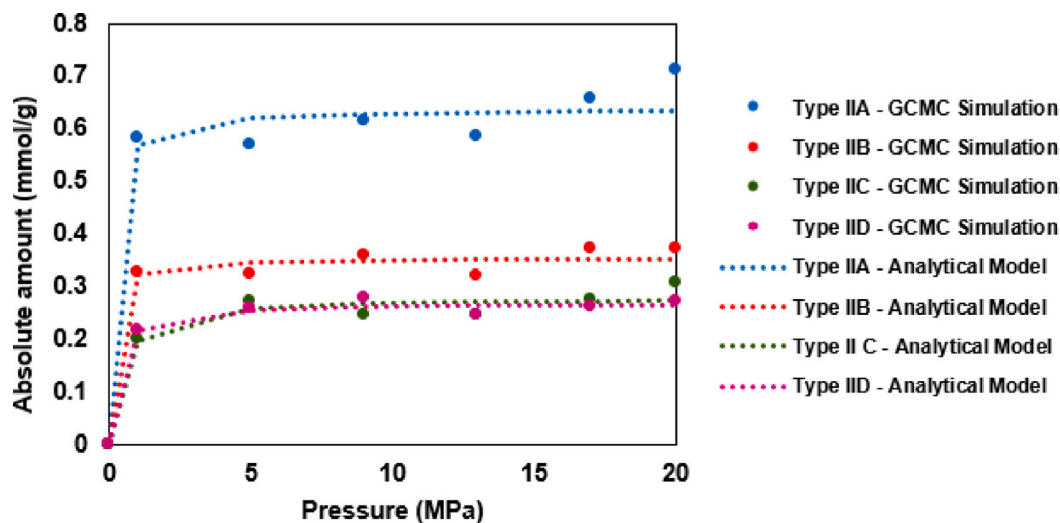


Fig. 8. Water adsorption isotherms at 300 K for kerogen type II at different thermal maturity levels.

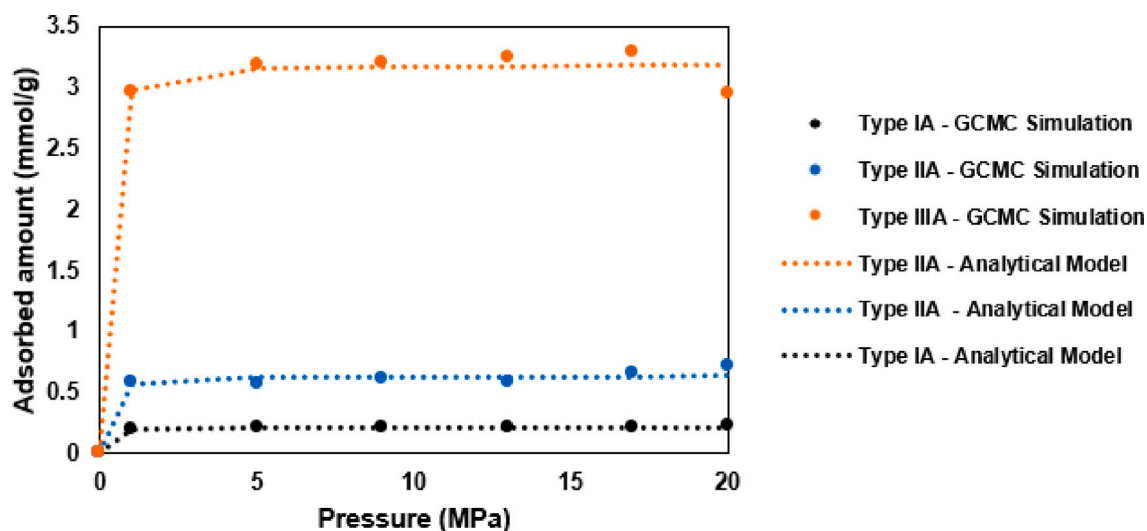


Fig. 9. Water adsorption isotherms at 300 K for different kerogen types.

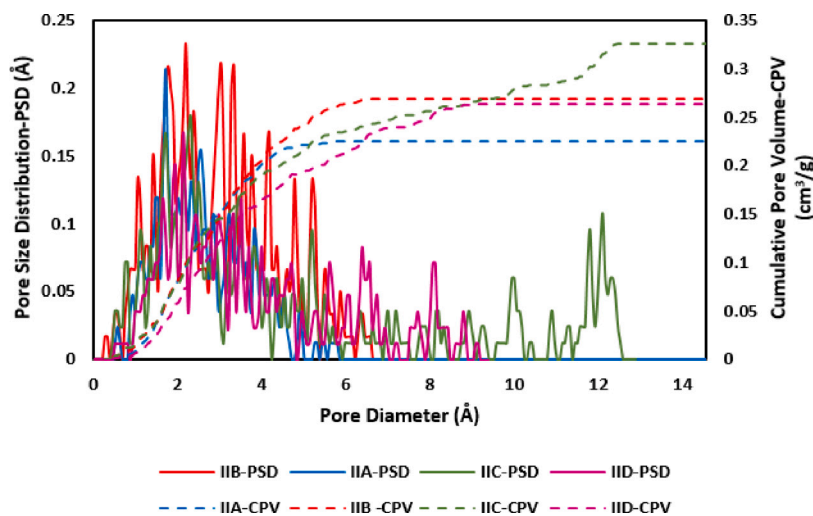


Fig. 10. Pore-size distribution and cumulative pore volume for kerogen structures IIA, IIB, IIC, and IID.

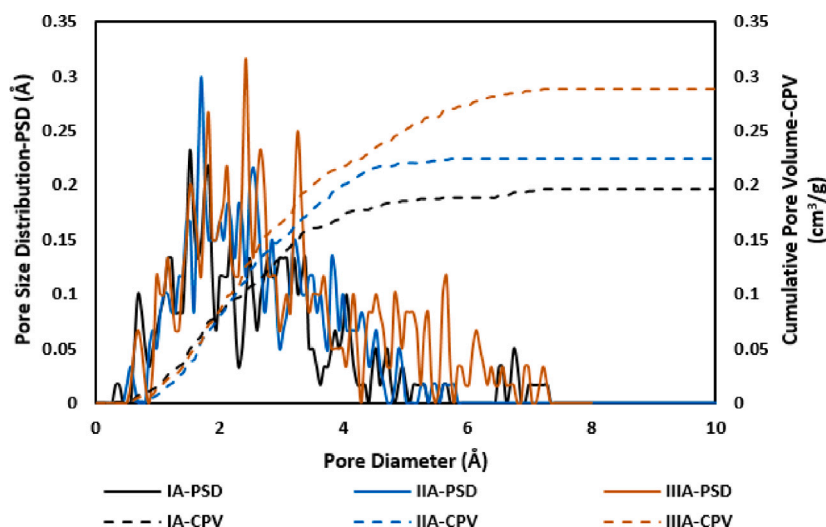


Fig. 11. Pore-size distribution and cumulative pore volume for kerogen structures IA, IIA, and IIIA.

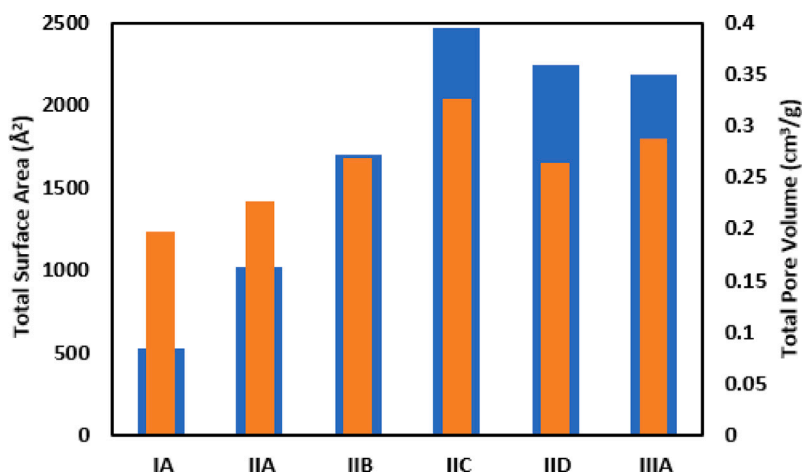


Fig. 12. Comparison of the total surface area and the total pore volume for all the kerogen structures.

We observe that the range of thermal maturity of kerogen results in different surface wettability of kerogen which directly impacts fluid flow in organic-rich mudrocks. For instance, kerogen structures with high surface affinity to gas lead to a decrease in gas mobility. The results presented in this work provide valuable insights about the adsorption behavior of water and gas on kerogen surfaces and confirms that kerogen geochemistry can significantly impact on the wetting behavior in organic-rich mudrocks. Additionally, the outcomes of this paper can contribute to the development of optimal field CO₂ injection processes for shale oil recovery as well as CO₂ storage in shale reservoirs by providing information about interaction of water and methane to kerogen, considering the influence of thermal maturity and type of kerogen. This knowledge can potentially be used to improve the calculation of adsorbed gas content on kerogen surface by taking into account the moisture content of kerogen.

Declaration of competing interest

The authors declare that they have no known competing financial interests or personal relationships that could have appeared to influence the work reported in this paper.

Data availability

No data was used for the research described in the article

Acknowledgments

The authors acknowledge the industry members of the University of Texas at Austin's Joint Industry Research Program on "Multi-Scale Rock Physics" sponsored by Core Laboratories, Equinor, ExxonMobil, Occidental Petroleum, Pan American Energy, Petrobras, and Woodside Energy for supporting this research. We also acknowledge the Texas Advanced Computing Center (TACC) at The University of Texas at Austin for providing High Performance Computing (HPC) resources which have contributed to the research results reported in this paper. A note of gratitude goes to the anonymous reviewers, the associate editor, and the managing editor of Fuel for their excellent technical and editorial feedback.

References

- [1] Van Krevelen DW. Coal typology - physics - chemistry - constitution. Elsevier 1961.
- [2] Ungerer P, Collet J, Yiannourakou M. Molecular modeling of the volumetric and thermodynamic properties of kerogen: Influence of organic type and maturity. Energy Fuels 2015;29(1):91–105. <http://dx.doi.org/10.1021/ef502154k>.
- [3] Orr WL, White CM. Analysis of maturity-related changes in the organic sulfur composition of kerogens by flash pyrolysis-gas chromatography. ACS Symposium Series 1990;429.

- [4] Kelemen SR, Afeworki M, Gorbati ML, Sansone M, Kwiatek PJ, Walters CC, Freund H, Siskin M, Bence AE, Curry DJ, Solum M, Pugmire RJ, Vandenbroucke M, Leblond M, Behar F. Direct Characterization of Kerogen by X-ray and Solid-State ¹³C Nuclear Magnetic Resonance Methods. *Energy & Fuels* 2007;21(3):1548–61. <http://dx.doi.org/10.1021/ef060321h>.
- [5] Baskin David K. Atomic H/C Ratio of Kerogen as an Estimate of Thermal Maturity and Organic Matter Conversion. *AAPG Bulletin* 1997;81:1437–50.
- [6] Vandenbroucke M, Largeau C. Kerogen origin. *Evol Struct Org Geochem* 2007;38(5):719–833. <http://dx.doi.org/10.1016/j.orggeochem.2007.01.001>.
- [7] Passy QR, Bohacs K, Esch WL, Klimentidis R, Sinha S. From oil-prone source rock to gas-producing shale reservoir-geologic and petrophysical characterization of unconventional shale gas reservoirs. In: Presented at the international oil and gas conference and exhibition in china. Beijing, China; 2010. <http://dx.doi.org/10.2118/131350-MS>, 8–10 June.
- [8] Sui H, Zhang F, Wang Z, Wang D, Wang Y. Effect of kerogen maturity, water content for carbon dioxide, methane, and their mixture adsorption and diffusion in kerogen: A computational investigation. *Langmuir* 2020;36(33):9756–69. <http://dx.doi.org/10.1021/acs.langmuir.0c01191>.
- [9] Xiao-Chun Lu, Fan-Chang Li, Watson A Ted. 1995,
- [10] Rivera José L, McCabe Clare, Cummings Peter T. Layering behavior and axial phase equilibria of pure water and water + carbon dioxide inside single wall carbon nanotubes. *Nano Letters* 2002;2(12):1427–31. <http://dx.doi.org/10.1021/nl0257566>.
- [11] Tang X, Ripepi N, Valentine KA, Keles C, Long T, Gonciaruk A. Water vapor sorption on marcellus shale: Measurement, modeling and thermodynamic analysis. *Fuel* 2017;209:606–14.
- [12] Tesson S, Firoozabadi A. Methane adsorption and self-diffusion in shale kerogen and slit nanopores by molecular simulations. *J Phys Chem C* 2018;122(41):23528–42. <http://dx.doi.org/10.1021/acs.jpcc.8b07123>.
- [13] Sui H, Yao J. Effect of surface chemistry for CH₄/CO₂ adsorption in kerogen: A molecular simulation study. *J Nat Gas Sci Eng* 2016;31:738–46. <http://dx.doi.org/10.1016/j.jngse.2016.03.097>.
- [14] Bousige C, Ghimbeu CM, Vix-Guterl C, Pomerantz AE, Suleimenova A, G. Vaughan, et al. Realistic molecular model of kerogen's nanostructure. *Nat Mater* 2016;15:576–82. <http://dx.doi.org/10.1038/nmat4541>.
- [15] Falk K, Pellenq R, Ulm FJ, Coasne B. Effect of chain length and pore accessibility on alkane adsorption in kerogen. *Energy Fuels* 2015;29:7889–96. <http://dx.doi.org/10.1021/acs.energyfuels>.
- [16] Michalec L, Lísál M. Molecular simulation of shale gas adsorption onto overmature type II model kerogen with control microporosity. *Mol Phys* 2017;115:1086–103. <http://dx.doi.org/10.1080/00268976.2016.1243739>.
- [17] Obliger A, Pellenq R, Ulm F-J, Coasne B. Free volume theory of hydrocarbon mixture transport in nanoporous materials. *J Phys Chem Lett* 2016;7:3712–7. <http://dx.doi.org/10.1021/acs.jpclett.6b01684>.
- [18] Ho TA, Criscenti LJ, Wang Y. Nanostructural control of methane release in kerogen and its implications to wellbore production decline. *Sci Rep* 2016;6(28053). <http://dx.doi.org/10.1038/srep28053>.
- [19] Feng F, Akkutlu IY. Molecular modeling of organic materials for flow simulation and digital source-rock physics. In: Presented at the SPE annual technical conference and exhibition. 2017.
- [20] Pathak M, Kwon M, Huang H. Kerogen swelling and confinement: Its implication on fluid thermodynamic properties in shales. *Sci Rep* 2017;7:12530. <http://dx.doi.org/10.1038/s41598-017-12982-4>.
- [21] Pathak M, Huang H, Meakin P, Deo M. Molecular investigation of the interactions of carbon dioxide and methane with kerogen: Application in enhanced shale gas recovery. *J Nat Gas Sci Eng* 2018;51:1–8. <http://dx.doi.org/10.1016/j.jngse.2017.12.021>.
- [22] Vasileiadis M, Peristeras LD, Papavasileiou KD, Economou IG. Modeling of bulk kerogen porosity: Methods for control and characterization. *Energy Fuels* 2017;31:6004–18. <http://dx.doi.org/10.1021/acs.energyfuels.7b00626>.
- [23] Wang Z, Li Y, Liu H, Zeng F, Guo P, Jiang W. Study on the adsorption, diffusion and permeation selectivity of shale gas in organics. *Energies* 2017;10(142). <http://dx.doi.org/10.3390/en10010142>.
- [24] Zhao T, Li X, Zhao H, Li M. Molecular simulation of adsorption and thermodynamic properties on type II kerogen: Influence of maturity and moisture content. *Fuel* 2017;190:198–207. <http://dx.doi.org/10.1016/j.fuel.2016.11.027>.
- [25] Huang Liang, Ning Zhengfu, Wang Qing, Qi Rongrong, Zeng Yan, Qin Huibo, Ye Hongtao, Zhang Wentong. Molecular simulation of adsorption behaviors of methane, carbon dioxide and their mixtures on kerogen: Effect of kerogen maturity and moisture content. *Fuel* 2018;211:159–72. <http://dx.doi.org/10.1016/j.fuel.2017.09.060>, <https://www.sciencedirect.com/science/article/pii/S0016236117311687>.
- [26] Collett J, Galliero G, Gouth F, Montel F, Pujol M, Ungerer P, et al. Molecular simulation and modelisation of methane/ethane mixtures adsorption onto a microporous molecular model of kerogen under typical reservoir conditions. *Microporous Mesoporous Mater.* 2014;197:194–203. <http://dx.doi.org/10.1016/j.micromeso.2014.06.016>.
- [27] Yiannourakou M, Ungerer P, Leblanc B, Rozanska X, Saxe P, Vidal-Gilbert S, et al. Molecular simulation of adsorption in microporous materials. *Oil Gas Sci Technol D'IFP Energ Nouvelles* 2013;68(6):977–94. <http://dx.doi.org/10.2516/ogst/2013134>.
- [28] Collett J, Ungerer P, Galliero G, Yiannourakou M, Montel F, Pujol M. Molecular simulation of bulk organic matter in type II shales in the middle of the oil formation window. *Energy Fuels* 2014;28(12):7457–66. <http://dx.doi.org/10.1021/ef5021632>.
- [29] Plimpton S. Fast parallel algorithms for short-range molecular dynamics. *J Comput Phys* 1995;117(1):1–19.
- [30] Dauber-Osguthorpe Pnina, Roberts Victoria A, Osguthorpe David J, Wolff Jon, Genest Monique, Hagler Arnold T. Structure and energetics of ligand binding to proteins: Escherichia coli dihydrofolate reductase-trimethoprim, a drug-receptor system. *Proteins: Structure, Function, and Bioinformatics* 1988;4(1):31–47. <http://dx.doi.org/10.1002/prot.340040106>.
- [31] Okiongo Kenneth S, Aplin Andrew C, Larter Steve R. Changes in Type II Kerogen Density as a Function of Maturity: Evidence from the Kimmeridge Clay Formation. *Energy & Fuels* 2005;19(6):2495–9. <http://dx.doi.org/10.1021/ef050194+>.
- [32] Archana, Jagadisan, Yang Anqi, Heidari Zoya. Experimental Quantification of the Impact of Thermal Maturity on Kerogen Density. *Petrophysics* 2017;58. SPWLA-2017-v58n6a4.
- [33] Zhang H, Bucior BG, Snurr RQ. Modelling and simulation in the science of micro- and meso-porous materials: molecular modeling of carbon dioxide adsorption in metal-organic frameworks. Elsevier; 2018, p. 99–149. <http://dx.doi.org/10.1016/B978-0-12-805057-6.00004-1>.
- [34] Dubbeldam D, Calero S, Ellis DE, Snurr RQ. RASPA: Molecular simulation software for adsorption and diffusion in flexible nanoporous materials. *Mol Simul* 2016;42(2):81–101. <http://dx.doi.org/10.1080/08927022.2015.1010082>.
- [35] Martin MG, Siepmann JI. Transferable potentials for phase equilibria. 1 united-atom description of n-alkanes. *J Phys Chem B* 1998;102(14):2569–77. <http://dx.doi.org/10.1021/jp972543+>.
- [36] Lorentz HA. Ueber die anwendung des satzes vom virial in der kinetischen theorie der gase. *Ann Phys* 1881;248(1):127–36. <http://dx.doi.org/10.1002/andp.18812480110>.
- [37] Berthelot D. Comptes rendus hebdomadaires des séances de l'académie des sciences. vol. 126, 1898, p. 1703–855.
- [38] Berendsen HJC, Grigera JR, Straatsma TP. The missing term in effective pair potentials. *J. Phys. Chem.* 1987;91(24):6269–71. <http://dx.doi.org/10.1021/j100308a038>.
- [39] Gelb LD, Gubbins KE. Pore size distributions in porous glasses: A computer simulation study. *Langmuir* 1999;15(2):305–8. <http://dx.doi.org/10.1021/la9808418>.
- [40] Alafnan S, Solling T, Mahmoud M. Effect of kerogen thermal maturity on methane adsorption capacity: A molecular modeling approach. *Molecules* 2020;25(16):3764. <http://dx.doi.org/10.3390/molecules25163764>.
- [41] Zhou Juan, Mao Qian, Luo Kai H. Effects of Moisture and Salinity on Methane Adsorption in Kerogen: A Molecular Simulation Study. *Energy & Fuels* 2019;33(6):5368–76. <http://dx.doi.org/10.1021/acs.energyfuels.9b00392>, PMID: 32063669.
- [42] Sing KSW. Reporting physisorption data for gas/solid systems with special reference to the determination of surface area and porosity (Recommendations 1984). *Pure Appl. Chem.* 1985;57(4):603–19. <http://dx.doi.org/10.1351/pac198557040603>.
- [43] Rouquerol Françoise, Rouquerol Jean, Sing Kenneth. CHAPTER 8 - Assessment of Microporosity. In: Rouquerol Françoise, Rouquerol Jean, Sing Kenneth, editors. *Adsorption by Powders and Porous Solids*. London: Academic Press; 1999, p. 219–36. <http://dx.doi.org/10.1016/B978-012598920-6/50009-9>, <https://www.sciencedirect.com/science/article/pii/B9780125989206500099>.
- [44] Dubinin MM, Serpinsky VV. Isotherm equation for water vapor adsorption by microporous carbonaceous adsorbents. *Carbon* 1981;19(5):402–3.
- [45] Muller EA, Rull LF, Vega LF, Gubbins KE. Adsorption of water on activated carbons: A molecular simulation study. *J Phys Chem* 1996;100:1189–96.
- [46] Jagadisan A, Heidari Z. Experimental quantification of the effect of thermal maturity of kerogen on its wettability. *SPE Reserv Eval Eng* 2019;22(04):1323–33. <http://dx.doi.org/10.2118/195684-PA>.